Boosting the oxygen evolution of high-entropy (oxy)hydroxide epitaxially grown on high entropy alloy by lattice oxygen activation

Yimin Zhang [a], Jianli Kang [a,*], Haonan Xie [a], Hongxia Yin [b], Zhijia Zhang [c], Enzuo Liu [a], Liying Ma [a], Biao Chen [a], Junwei Sha [a], Lihua Qian [b], Wenbin Hu [a], Chunnian He [a], Naiqin Zhao [a,*]

[a] School of Materials Science and Engineering, Tianjin University, Tianjin 300350, PR China
[b] School of Physics, Huazhong University of Science and Technology, Wuhan 430074, PR China
[c] School of Materials Science and Engineering, Tiangong University, Tianjin 300387, PR China

ARTICLE INFO

ABSTRACT

The unique electronic structure and diverse elemental composition of high-entropy materials (HEMs) have already showcased remarkable properties in the realm of oxygen evolution reaction (OER). Despite this, the active sites and reaction pathways of HEMs have yet to be fully understood. Our findings indicate that the addition of Fe in HEMs results in a more positive valence state of metals, leading to the enhancement of the covalent characteristic of the M-O bond. Additionally, the predominant oxygen 2p orbitals near the Fermi level enables lattice oxygen to function as an OER center. Guided by theoretical calculations, we synthesized a nanoporous NiFeCoMnOOH (np-NiFeCoMnOOH) electrocatalyst exhibited a low overpotential of 194 mV at 10 mA cm^{-2} and long-term stability of 120 h at 100 mA cm^{-2}. These results offer insights into the reaction mechanisms of HEM electrocatalysts and may guide future studies in designing high-entropy electrocatalysts with superior activity.

1. Introduction

The development of new energy technologies is a top priority for many countries and regional organizations, as it is necessary to solve the problems caused by the environmental pollution, energy crisis, and harmful effects of burning fossil fuels [1–3]. The oxygen evolution reaction (OER) is a fundamental half-reaction in many electrochemical applications, such as water splitting, carbon dioxide reduction reaction (CO_2RR) and rechargeable metal-air batteries [4,5]. However, the sluggish four-electron transfer process of the OER limits the power and energy efficiency in such approaches [6–8]. Based on this status, it is urgent to design OER electrocatalysts with high catalytic performance and excellent stability.

The exceptional catalytic performance of OER electrocatalysts is founded on thorough understanding of their mechanisms and reaction paths. The OER process is typically divided into four steps: adsorption, deprotonation, coupling, and release of oxygen-containing intermediates. This is commonly known as the adsorption evolution mechanism (AEM) [9]. However, AEM pathway has a significant

theoretical overpotential (0.37 V), which is limited by the binding energy of the active site with the intermediates [10]. Recently, an advanced Lattice Oxygen Oxidation Mechanism (LOM) has been proposed, which bypasses the traditional rate-determining step (O-O bond formation (OOH*)) in AEM, thus providing more efficient OER processing [11–13]. However, the larger electronegativity of oxygen makes its reduction thermodynamically unfavorable due to its energy band is deeper level in the energy diagram [14]. Due to the electronic variation caused by the highly oxidized state of the metal, the nd band is lowered [15,16]. As a result, the orbital hybridization becomes very strong, leading to high covalency of the M-O bond. Additionally, the large charge deviation between the highly oxidized metal atoms and the O ion results in the intramolecular electron transfer that form ligand cavities. This process increases the amount of non-bonded oxygen [17–19]. This is generally considered to be an important strategy to activate LOM [20–24]. Based on this strategy, recent studies report that introducing the high-valent metal of Mo promotes the lattice oxygen activity of NiFeLDH [23,25]. And, some researchers studied the OER route variations in $Zn_xCo_{1-x}OOH$ [13], found that the doping of Zn increased the

oxidation state of Co, leading to the conversion of AEM to LOM mechanism. Meanwhile, researchers have studied how non-metallic elements can transform the reaction path[26]. Among these, electronically complex transition metal Ni, Co and Mn-based multi-metal electrocatalysts have shown some LOM pathway tunability [13,27,28]. However, active sites and reaction pathways for NiCoMn ternary composites are still lacking [29,30]. Meanwhile, identification of active sites and reaction pathways becomes more challenging as the number of elements and complexity of electronic structures increase, as in the case of high entropy materials (HEMs) electrocatalysts. So far, the origin of the catalytic activity for HEMs is often limited by the advance definition of active site and the simplification of catalyst models [31–33]. Consequently, it still remains a challenging and rewarding task to elucidate the bottlenecks in HEM electrocatalysts due to the complexity of elemental species and electronic structure, based on the transformation of the reaction mechanism and OER performance.

With the above question in mind, we investigated in detail the transition behaviour of NiCoMnOOH and NiFeCoMnOOH electrocatalysts in the active site and reaction pathways in OER, and found that the elevated metal binding energy due to Fe in HE (oxy)hydroxide is the key to the activation of LOM. More specifically, the dual-metal-site mechanism with Ni-Fe as the active site on the surface is at the centre of LOM, while the O2p orbitals closer to the Fermi energy level facilitate the LOM process. Based on the theoretical guidance, we have prepared a corresponding np-NiFeCoMnOOH catalyst by surface reconstruction of nanoporous NiFeCoMn precursor. Experimental results show that the OER proceeds readly via LOM pathway on the np-NiFeCoMnOOH catalyst and exhibit excellent OER performance, showing low overpotential of 194 mV at the current density of 10 mA cm^{-2}, which have the obviously advantage than RuO$_2$. This work not only advances our understanding of the catalytic mechanisms involved in the OER reaction process in high-entropy electrocatalysts but also highlights new approaches to achieving better high-entropy electrocatalysts through the construction of relationships between elemental composition and microstructure and catalytic activity.

2. Experimental section

2.1. Preparation of nanoporous electrocatalyst

The ere-NiFeCoMn and ere-NiCoMn ingots were obtained by arc melting with pure metals Ni, Fe, Co and Mn in an argon atmosphere over 3 times. Then, the ingots were melted again in a quartz tube and ejected onto a Cu roll at 1400 rpm for rapid solidification to form the alloy stripes.

All nanoporous electrodes are prepared by a convenient alloying/dealloying process. Ingots were obtained by arc melting with pure metals Ni, Fe, Co and Mn in an argon atmosphere over 3 times. Then, the ingots were melted again in a quartz tube and ejected onto a Cu roll at 1400 rpm for rapid solidification to form the precursor alloys. Nanoporous NiFeCoMn, nanoporous NiCoMn and nanoporous NiMn precursor electrocatalysts prepared by controlled electrochemical dealloying using the three-electrode system with graphite rods as counter electrode and Ag/AgCl as reference electrode in 1 M (NH$_4$)$_2$SO$_4$, followed by repeatedly and thoroughly rinsed with alcohol and ultrapure water (18.2 MΩ). The np-NiFeCoMnOOH, np-NiCoMnOOH and np-NiMnOOH were in situ activated by 200 turns of cyclic voltammogram (CV) curves in the voltage window from 0.2 to 0.6 V (vs. Hg/HgO) in 1 M KOH.

For comparison, RuO$_2$ catalyst ink was prepared by dispersing the mixture of the sample (4 mg) with VulcanXC-72 carbon (1 mg) into 1 ml mixed solution (5 % Nafion solution/deionized water/isopropanol = 4:96:25 in volume). Then 10 μL of homogeneously mixed catalyst ink was coated on a polished glassy carbon electrode (0.196 cm^2) and dried in ambient air for the following electrochemical testing.

2.2. Structural characterizations

The microstructure and morphology of as-prepared samples were presented by SEM (FE-SEM, S-4800), TEM (JEOL JEM-2100 f), and double AC-TEM (FEI Titan Themis G2) operating at 60 kV. XRD (Bruker D8 Advanced) measurements equipped with Cu Kα radiation were recorded to reveal the crystal structure. To reflect the chemical state of each element in the as-prepared materials, XPS characterization was carried out on Kratos Axis Supra. The phase composition and chemical bonding properties in the samples are characterized by Raman spectroscopy (RAMAN, Renishaw inVia). The spot size of the laser for Raman spectroscopy is 0.9 μm. The wavelength of the laser for Raman spectroscopy is 532 nm. The power of the laser for Raman spectroscopy is 90 mW.Raman spectrometer with a 532 nm laser.

2.3. Electrochemical measurements

The platinum electrode was thoroughly surface cleaned by 1000 turns of CV curves in the voltage window from − 2 to 2 V (vs. Ag/AgCl) in 0.5 M H$_2$SO$_4$ solution, after which potential calibration experiments were carried out in H$_2$-saturated electrolyte (1 M KOH) with a clean platinum sheet as the working electrode. The electrochemical measurements were carried out in classical three-electrode system with graphite rods as counter electrode, Hg/HgO electrode as reference electrode, and self-supported nanoporous OER electrocatalytic materials as working electrodes. To ensure accurate comparisons, all overpotentials were tested under the same conditions. The working electrodes, electrolyte, sweep speed, and other experimental parameters were kept consistent throughout the experiments. The OER polarization curves of electrodes were measured in O$_2$-saturated 1 M KOH (electronic grade) solution, except for the solution-dependent experiments. Polarization curve was taken at a scan rate of 1 mV s^{-1} and the potential at $i = 0$ was used as the thermodynamic equilibrium potential for the hydrogen evolution reaction. The electrical potential data obtained from the tests were corrected to RHE according to the equation, $E_{RHE} = E_{Hg/HgO} + 0.920$ V. EIS measure at the overpotential of 200 mV with frequency ranging from 0.01 Hz to 100 kHz, meanwhile, iR-corrected potential using the resistance of the electrolyte R_s from the EIS measure result according to the equation, $E_{corr} = E_{Hg/HgO} + 0.920 - iR_s$ V. The stability of the electrocatalyst was judged by using the chronopotentiometry method at 10 mA cm^{-2} and 100 mA cm^{-2} current densities for 120 h, respectively. Double-layer capacitance (C$_{dl}$) values were obtained by fitting CV data collected for all electrodes in the voltage window of 0.18–0.28 V (vs. Hg/HgO) at different scan rates.

3. Results and discussion

To thoroughly examine the disparities in active sites and reaction mechanisms, AEM and LOM, in OER electrocatalysts with multi-metal (oxy)hydroxides (Fig. 1a and Fig. S1), the theoretical calculations were conducted to ascertain the active centers and pathways of both NiCoMnOOH and NiFeCoMnOOH.

In the AEM reaction pathway, the presence of complex HEMs necessitates that we limit the active center to the metal sites (including Ni, Fe, Co, and Mn) on the electrocatalyst surface. On the other hand, in the LOM reaction pathway, the active center is composed of the oxygen atom located between the different metals (such as Fe, Co and Mn) and Ni [34]. To model the multielement electrocatalyst in DFT calculations, we performed Ni metal atom substitution on the β-NiOOH (001) surface.

Theoretical calculations suggest that NiCoMnOOH and NiFeCoMnOOH electrocatalysts display distinctive reaction activity sites in the AEM pathway (Fig. S2 and Fig. 1b). For both types of electrocatalysts, the deprotonation of *OH, happening at metal active sites, represents the potential determining step (PDS) for OER following the AEM pathway. Notably, the NiCoMnOOH electrocatalyst features the Co site having the lowest reaction energy barrier, measuring at 0.834 V,
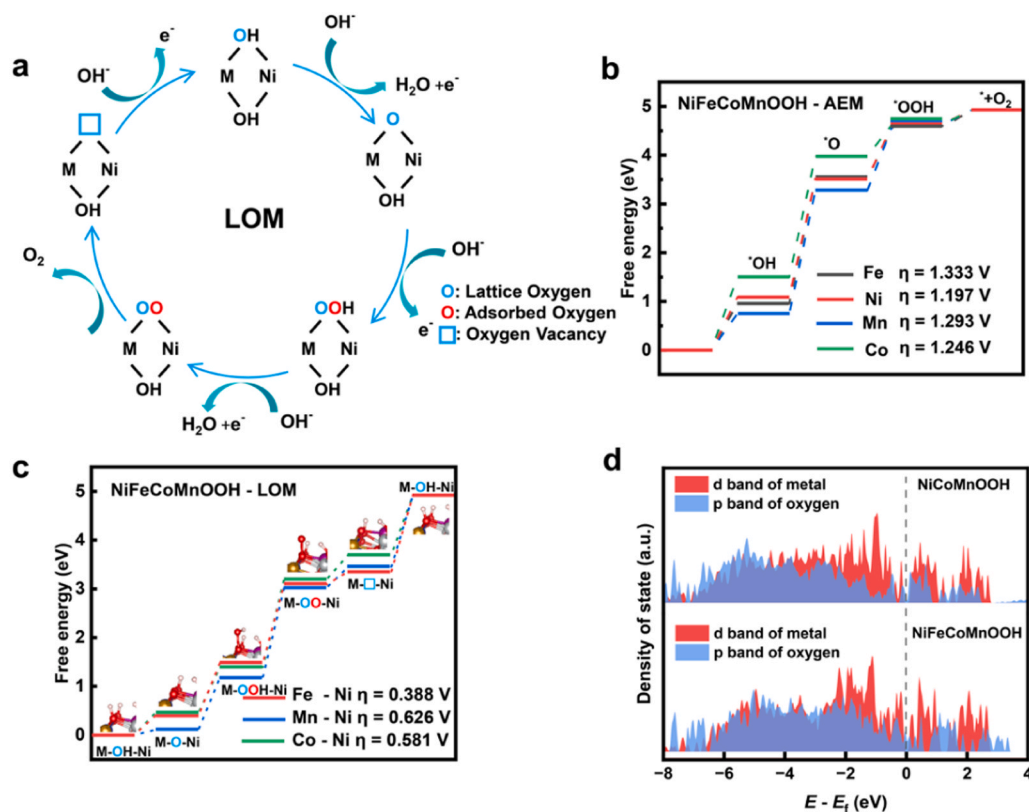
Fig. 1. Theoretical calculation of OER reaction mechanism. a Schematic illustration of LOM pathway. b AEM and c LOM on NiFeCoMnOOH surface at a potential of 0 V. d Density of state (DOS) of NiCoMnOOH and NiFeCoMnOOH electrocatalysts.

while with the introduction of Fe, Ni replaces Co as the new active site, but the corresponding reaction energy barrier increases to 1.197 V. This illustrates that the AEM reaction mechanism is more challenging to transpire in NiFeCoMnOOH than in NiCoMnOOH during the OER.

The LOM pathway initiates the catalytic reaction through deprotonating the hydroxyl group between the dual-metal-site atoms on the (oxy)hydroxide surface (step 1) (Fig. 1a). Subsequently, the OH$^-$ ions in solution combine with the deprotonated lattice oxygen to form *OOH (step 2). The secondary deprotonation process forms *OO on the surface, which is subsequently released from the crystal lattice in the form of O_2 (step 3), generating oxygen vacancies on the surface (step 4). Finally, the surface oxygen vacancies are occupied by OH$^-$ ions, resulting in the reversal of the (oxy)hydroxide structure to its original state (step 5). Free Energy diagrams of OER calculated through the LOM pathway on NiFeCoMnOOH and NiCoMnOOH electrocatalysts are shown in Fig. 1c and Fig. S3. For the NiCoMnOOH, the combine of lattice oxygen with OH$^-$ ions as PDS generates a potential barrier of 0.928 V. On the other hand, the introduction of Fe significantly activates the lattice oxygen on the catalyst surface, resulting in the PDS on the NiFeCoMnOOH towards deprotonation of *OOH, and resulting in a reduction in the energy barrier change to 0.388 V. Changing the reaction mechanism from AEM to LOM allows NiFeCoMnOOH to exhibit a lower reaction energy barrier and a significant advantage over NiCoMnOOH. The density of state (DOS) diagram enables detailed information of the electron band configuration for each element in the electrocatalyst, which is difficult to measure experimentally. As shown in Fig. 1d, there are regions of overlap between the D-band of the metal and the p-band of the oxygen, indicating a covalent hybridization between the metal atoms and the oxygen ligands. Noteworthy, after the metal element Fe was added to the electrocatalyst, the increased distribution of electronic states near the Fermi level (E_f) indicating that the NiFeCoMnOOH electrocatalyst can favours electron transfer during the reaction and improve the reaction rate [35]. Meanwhile, for the NiCoMnOOH, d band center of

metal closer to the E_f, indicating that the metal elements as the redox center, which is consistent with the theoretical-calculated PDS of AEM and LOM. As the Fig. S4 shown, the O 2p orbital center of NiFeCoMn positively shifted by 0.44 eV compared to NiCoMn and its domination near E_f promote the lattice oxygen redox reactions, making it central to the LOM [36]. Meanwhile, as the Fig. S5 shown, the down shifted ICOHP between Ni and O (from −1.740 to −1.857) dur to the addition of Fe. This suggests that the higher activity of lattice oxygen is more conducive to the occurrence of LOM processes [25]. The charge differences density (Fig. S6) and pDOS (Fig. S7) results also indicate that compared to NiCoMnOOH, oxygen in NiFeCoMnOOH is more prone to becoming reactive active centers. Thus, the theoretical calculations predict that the addition of Fe can alter the reaction pathway of NiCoMnOOH electrocatalyst and improve its OER activity.

To verifying the theoretical calculation results, strips of NiCoMn and NiFeCoMn with nearly equal ratios of elemental constituents, labeled ere-NiCoMn and ere-NiFeCoMn respectively (Fig. S8 and S9), were produced through the process of melt spinning. Additionally, considering the surface oxidation of catalysts during the OER [37,38], in-situ Raman techniques were employed to visualize the transformation of the multi-metal (oxy)hydroxide catalysts and study their surface reconstruction procedure. Near the 468 and 550 cm^{-1}, two characteristic Raman signals of Ni^{3+}-O are gradually identified on the recorded spectra with elevated potentials (Fig. 2a, b), which are associated with the bending vibration E$_g$ (δ (Ni-O)) and stretching vibration A$_{1\,g}$ (ν (Ni-O)) modes in NiOOH, respectively [39]. As shown in Fig. 2a and b, the Raman signals of ere-NiCoMn remained stable, while the ere-NiFeCoMn catalyst revealed a clear NiOOH characteristic signal at 1.27 V (vs. RHE), indicating that the presence of Fe in these electrocatalysts could reduce the voltage for (oxy)hydroxide formation, leading to the emergence of active materials and increased catalytic activity. Moreover, the characteristic Raman bands of ere-NiFeCoMn were significantly blue-shifted relative to those of ere-NiCoMn (Fig. 2a, b),
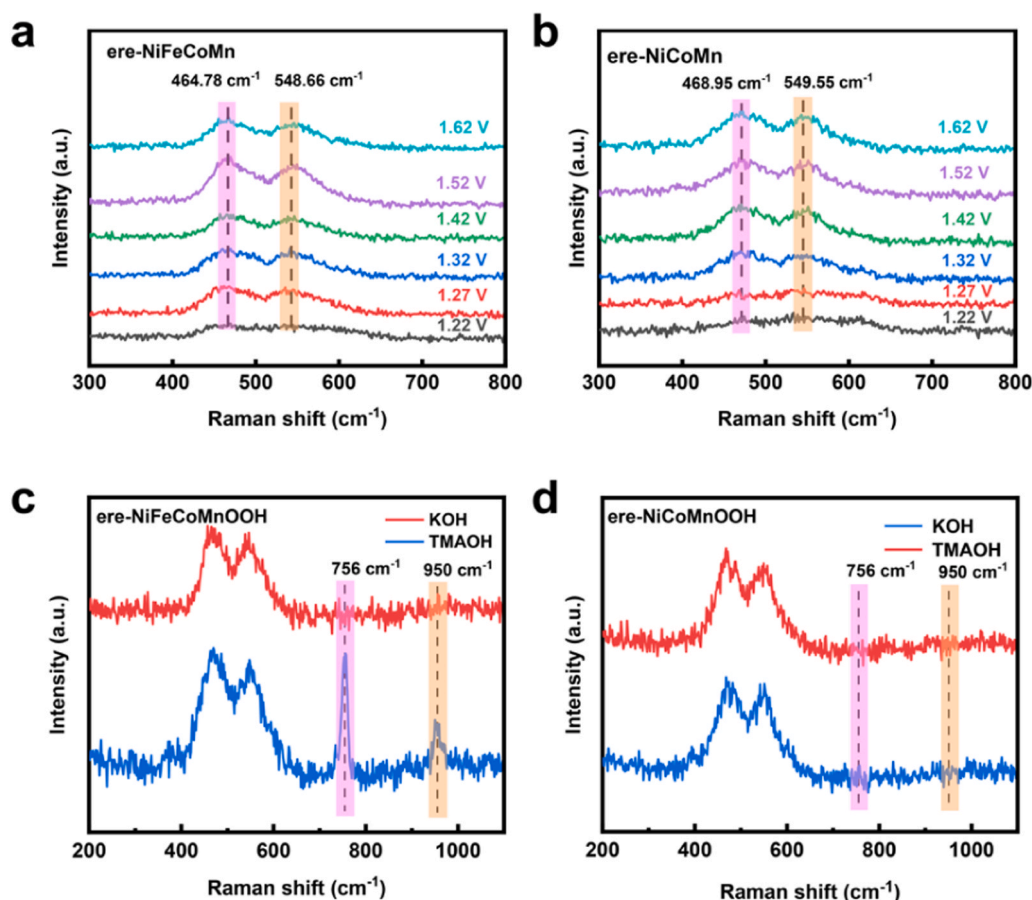
Fig. 2. Understanding of improved OER performance and reaction mechanisms. a, b Electrochemical in situ Raman spectra of ere-NiFeCoMn and ere-NiCoMn at the range of 300–700 cm^{-1} at the operated potentials from 1.22 to 1.62 V vs. RHE. c, d Raman spectra of ere-NiFeCoMnOOH and ere-NiCoMnOOH electrocatalyst. Both of ere-NiFeCoMnOOH and ere-NiCoMnOOH were respectively operated at 1.55 V vs. RHE in 1 M KOH (red line) and 1 M TMAOH (blue line) solution for 20 min. Then, electrocatalysts was cleaned by thoroughly washing with DI water and acetone for the measurements of ex-situ Raman spectrum.

suggesting notable lattice distortion in ere-NiFeCoMn, leading to the formation of HE (oxy)hydroxide of the ere-NiFeCoMnOOH and ere-NiCoMnOOH variety.

To distinguish the different OER pathways of the two electrocatalysts, the chemical identification method was used to demonstrate the presence of negatively charged peroxo-like species $O_2^{\delta-}$ (such as O_2^{2-} and O_2^-) during the LOM reaction. Tetramethylammonium cations (TMA$^+$) have unique interaction properties with $O_2^{\delta-}$ and can bind strongly to the surface of the OER electrocatalyst which followed LOM [40] as shown in the Fig. S10. Therein, both of the electrocatalysts were operated at 1.55 V vs. RHE in 1 M TMAOH solution for 20 min, then, the electrocatalyst was cleaned by DI water and acetone for the measurements of ex-situ Raman spectrum. Fig. 2d illustrates that two clear peaks appeared at 756 and 950 cm^{-1} which coincide with the characteristic peaks of TMA$^+$, whereas the characteristic peak of TMA$^+$ found near 454 cm^{-1} is not evident due to the presence of the ere-NiFeCoMnOOH. This observation suggests that, unlike ere-NiCoMnOOH, ere-NiFe-CoMnOOH follows the LOM reaction pathway for the OER. This is in contrast to ere-NiCoMnOOH, as indicated by the absence of a clear distinction in Fig. 2d.

In order to enhance the number of active sites, we prepared a nanoporous NiFeCoMn high-entropy alloy precursor (np-NiFeCoMn precursor) via electrochemical dealloying, which was in situ activated through cyclic voltammetry (CV) to form a free-standing composite electrode (np-NiFeCoMnOOH) (Scheme 1, Supplementary information). X-ray diffraction (XRD) of the Ni$_x$Fe$_x$Co$_x$Mn$_{50}$ (x = 50/3) HEA precursor exhibits four obvious peaks at 43.14, 50.22, 73.67 and 89.44°, corresponding to the conventional face-center cubic (FCC) phase (Fig. S11).

The elemental composition of the HEA precursor was determined using energy-dispersive X-ray spectroscopy (EDS) of the scanning electron microscope (SEM), which showed consistency with the initial design composition (Fig. S12). Subsequently, the np-NiFeCoMn precursor was synthesized by controlled electrochemical dealloying method in 1 M (NH$_4$)$_2$SO$_4$ at − 0.49 V (vs. Al/AgCl) for 5 h. There appears a new peak at 38.22° in addition to the four characteristic peaks of the np-NiFeCoMn precursor after surface reconstruction, which should contribute to the (1 0 2) plane of nickel (oxy)hydroxide (PDF-#06-0075) (Fig. 3a and Fig. S13). This finding was supported by the in-situ Raman results. Meanwhile, the lattice distortion caused by the high-entropy effect leads to a slight widening of the crystal plane spacing in the NiFeCoMnOOH compared to the NiOOH.

The SEM images (Fig. 3b and Fig. S14) demonstrates that the np-NiFeCoMn precursor electrocatalyst surface consists of a nanoporous structure with a diameter of ~15 nm. N$_2$ adsorption-desorption measurements further demonstrates that np-NiFeCoMnOOH electrocatalyst has a large specific surface area (11.471 m^2 g^{-1}) (Fig. S15). Meanwhile, the TEM images in Fig. S16 clearly reveals the microscopic morphology of the np-NiFeCoMn precursor. The controlled degree of the electrochemical dealloying process accounts for the self-support properties of the material and greatly increases the specific surface area of the electrocatalyst, effectively facilitating the electrochemical reactio n[41,42]. As shown in Fig. 3c, ultra-thin NiFeCoMnOOH were uniformly grown on the surface of np-NiFeCoMn precursor electrocatalyst after surface reconstruction process. Similar microstructures were observed on ere-NiFeCoMnOOH by SEM and TEM (Fig. S17). TEM analysis further reveals the relationship between the nanoporous metal and the HE (oxy)
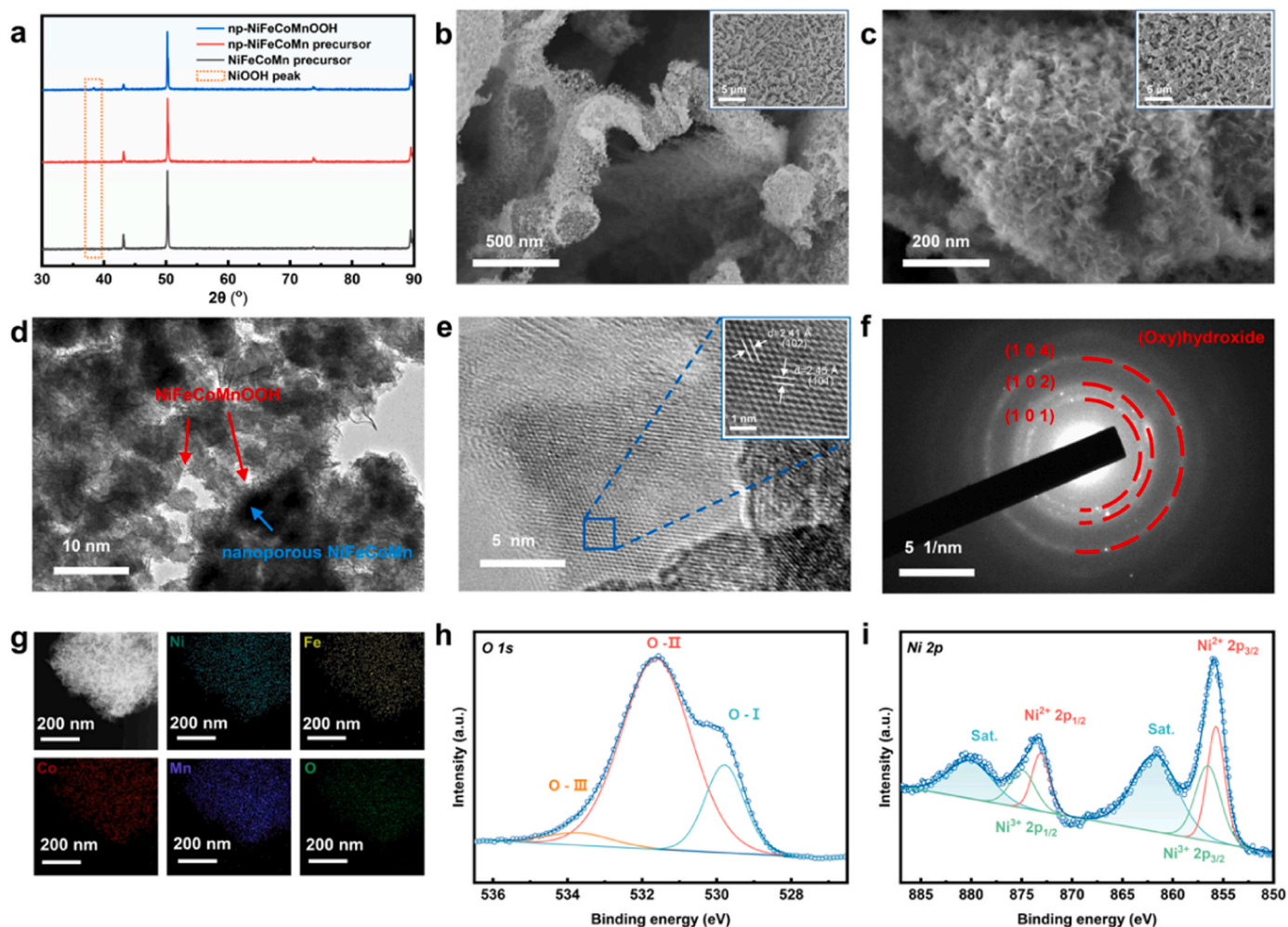
Fig. 3. Microstructure and chemical composition of np-NiFeCoMnOOH electrocatalysts grown on nanoporous NiFeCoMn precursor. a X-ray diffraction (XRD) patterns of NiFeCoMn precursor, np-NiFeCoMn precursor and np-NiFeCoMnOOH. Typical Scanning Electron Microscopy (SEM) images of b the np-NiFeCoMn precursor and c the np-NiFeCoMnOOH electrocatalyst surface with ultra-thin NiFeCoMnOOH after the surface reconstruction. d Transmission Electron Microscopy (TEM) image of the np-NiFeCoMnOOH electrocatalyst. e High-resolution transmission electron microscopy (HRTEM) image of the NiFeCoMnOOH. f Selected area electron diffraction (SAED) patterns of the np-NiFeCoMnOOH electrocatalyst. g Elemental mapping showing the uniform distribution of Ni, Fe, Co, Mn and O elements in the np-NiFeCoMnOOH electrode. X-ray photoelectron spectroscopy (XPS) spectra of h O 1s and **i** Ni 2p in the np-NiFeCoMnOOH electrode.

hydroxides (Fig. 3d). This unique structure ensures high exposure of the active site and fast charge transfer for electrocatalytic reactions. The high-resolution transmission electron microscopy (HRTEM) image (Fig. 3e) confirms the NiFeCoMnOOH structure and displays lattice planes with interplanar spacing of 2.41 and 2.45 Å, corresponding to the lattice planes of (102), (101) in (NiFeCoMn)OOH, respectively. The high crystallinity indicates that the NiFeCoMnOOH generated by surface reconstruction have a more stable structure, providing the basis for the long-lasting stability of the electrocatalyst. The selected area electron diffraction (SAED) patterns (Fig. 3f) of the electrocatalyst display similar (101), (102), and (1014) diffraction rings of NiOOH. The uniform distribution of Ni, Fe, Co, Mn and O in np-NiFeCoMnOOH is demonstrated by the energy dispersive X-ray mapping (Fig. 3g and Fig. S18). The self-supporting properties of the electrocatalyst, effectively reducing the use of binder, are clearly demonstrated in macroscopic photographs of the material (Fig. S19). Meanwhile, the X-ray photoelectron spectroscopy (XPS) spectra of O 1 s has three characteristic peaks labelled O-I, O-II and O-III assigned to M-O, oxygen in M-OH, and H_2O, respectively (Fig. 3h). Additionally, the XPS spectra of Ni, Co, Fe, and Mn 2p recorded in the np-NiFeCoMnOOH electrode indicate characteristic (oxy)hydroxide features (Fig. 3i and Fig. S20) indicative of the highly oxidized states of the metal elements present on the surface of the

electrocatalyst. Meanwhile, due to the distinction in the ability of the different atoms to attract electrons, Fe element's oxidation state is + 3, while the Ni and Co elements' oxidation state are between + 2 and + 3. Overall, the np-NiFeCoMnOOH electrocatalyst's unique nanoporous structure and surface morphology, provides the basis for highly efficient electrocatalytic reactions.

The significance of the structures in np-NiFeCoMnOOH catalysts was investigated by evaluating the OER performance of ere-NiFeCoMnOOH in O_2-saturated 1 M KOH electrolytes using a conventional three-electrode setup. Fig. 4a clearly illustrates the advantages of the nanoporous structure in the OER process. The np-NiFeCoMnOOH catalyst exhibited a significantly smaller onset overpotential than the ere-NiFeCoMnOOH, indicating effective improvement of the electrochemical performance when using catalysts with a three-dimensional structure. Subsequently, studies of the kinetic parameters (Tafel slope) and Cdl followed (Fig. S21). The Tafel slope of ere-NiFeCoMnOOH slightly increased compared to np-NiFeCoMnOOH, demonstrating that the microstructure design of the catalysts could effectively enhance the electrocatalytic reaction velocity. Moreover, there was a dramatic change in the Cdl of the materials, suggesting that the nanoporous structure can expose more electrochemically active sites. The result of the EIS study indicated that the unique microstructure facilitates charge
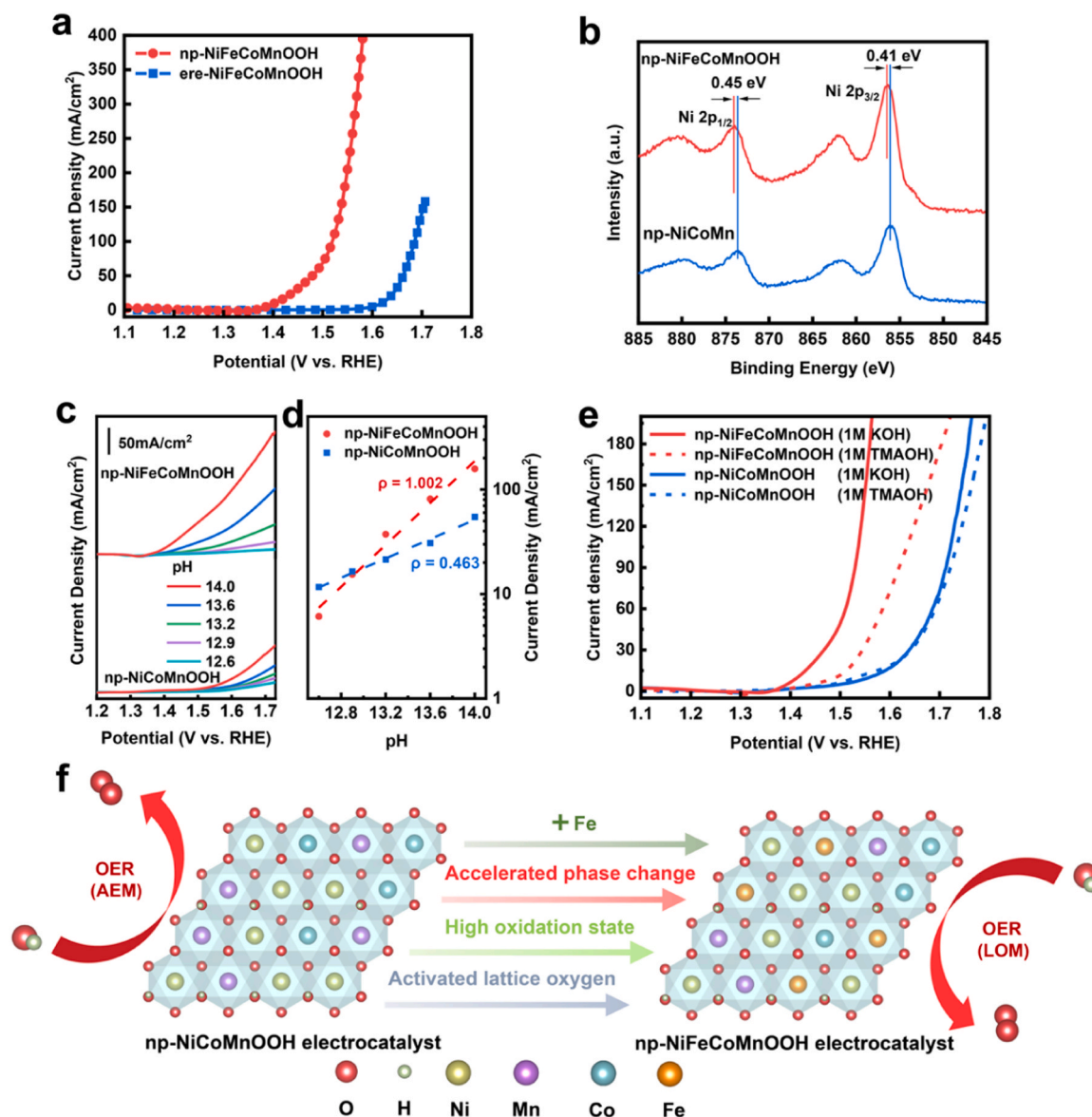
Fig. 4. OER mechanism revealed by pH dependence and chemical identification method. a OER linear sweep voltammetry (LSV) curves for np-NiFeCoMnOOH and ere-NiFeCoMnOOH electrocatalyst in 1 M KOH (electronic grade) with iR-corrected. Scan rate: 5 mV s^{-1}. b XPS spectra confirmed the increase in the valence state of Ni by a positive shifted binding peak. c LSV curves for np-NiFeCoMnOOH and np-NiCoMnOOH electrocatalyst measured in KOH with pH = 12.6, 12.9, 13.2, 13.6 and 14.0. d OER current density at 1.60 V vs. RHE drew in log scale as a function of pH, from which dependency relationship ($\rho = d\log i/d$pH) between the catalytic performance of different catalysts and the pH were calculated. e LSV curves for np-NiFeCoMnOOH and np-NiCoMnOOH electrocatalyst measured in 1 M KOH and 1 M TMAOH. f The schematic illustration of efficient oxygen evolution of HE (oxy)hydroxide.

exchange in catalytic reactions and reduces the electrical energy consumption (Fig. S22). As a contrast, the np-NiFeCoMnOOH and np-NiCoMnOOH (synthesized by the same method with np-NiFeCoMnOOH) catalysts were also studied by XPS to contrast the electronic states of metal components (Fig. 4b and Fig. S23). As other metal elements, the XPS spectra confirmed the increase in the valence state of nickel by a positive shifted binding peak of approximately 0.41 eV (Fig. 4b). This change in binding energy arises from the gap between the more electronegative Fe^{3+} (1.651) and the less electronegative Ni^{2+} (1.367) and Co^{2+} (1.377) [43], it is also shown that the addition of elemental Fe increases the binding energy of the surface metal, thereby enhancing the M-O covalent bonding properties and activating lattice oxygen [44].

In general, the performance of OER catalysts, which follow the LOM reaction process, is experimentally dependent on the pH of the solution. To evaluate the OER catalytic performance of the np-NiFeCoMnOOH

and np-NiCoMnOOH catalysts, experiments were conducted at various pH levels (14.0, 13.6, 13.2, 12.9 and 12.6), as shown in Fig. 4c. Fig. 4d demonstrate the dependency relationship between the catalytic performance of different catalysts (np-NiFeCoMnOOH and np-NiCoMnOOH) and the solution pH, obtained by fitting the current density at 1.6 V vs. RHE in log scale with the solution pH values ($\rho = d\log i/d$pH). The significantly different dependencies ($\rho_{NiFeCoMn}=1.002$ and $\rho_{NiCoMn}=0.463$) indicate a clear difference between the electron transfer and proton transfer kinetics of the different catalyst species, Therefore, the np-NiFeCoMnOOH and np-NiCoMnOOH electrocatalysts follow diverse reaction pathways in the OER.

On the other hand, it can be seen from Fig. 4e that the OER electrocatalytic activity retention capacity of np-NiFeCoMnOOH was considerably lower than that of np-NiCoMnOOH under different solutions (1 M KOH and 1 M TMAOH). Additionally, the Tafel slopes, which characterize the electrochemical reaction kinetics, exhibit similar

phenomena. As the Fig. S24 shows, the Tafel slops of np-NiFeCoMnOOH at the 1 M KOH (67.96 mV/dec) is increased by 97.46 % while the increase for np-NiCoMnOOH is just 7.51 %, indicating that the unique interaction properties between TMA$^+$ and O$^{2\delta-}$ severely inhibited the LOM during the OER for np-NiFeCoMnOOH electrocatalyst. Additionally, the combination of ^{18}O-isotope labeling with gas chromatography-mass spectrometer (GC-MS) results provides a more direct confirmation of the change in the reaction pathway (Fig. S25). Thus, the above analysis demonstrates the conversion of the OER mechanism from the AEM to the LOM pathway with the introduction of Fe (Fig. 4f).

To assess the electrocatalytic activities of the free-standing np-NiFeCoMnOOH composite electrode, the OER activity were assessed in O$_2$-saturated 1 M KOH electrolytes using a conventional three-electrode setup. For comparison, np-NiCoMnOOH and np-NiMnOOH electrodes, synthesized by the same method, as well as the benchmark RuO$_2$ catalyst, were also measured side by side. The reference electrode of Hg/HgO has been calibrated in advance for all electrochemical tests (Fig. S26). Generally, the overpotential achieves a current density of 10 mA cm^{-2} is commonly used to discriminate the performance of an electrocatalyst [45]. As shown in the linear sweep voltammetry (LSV) curves (Fig. 5a), the np-NiFeCoMnOOH catalyst exhibit the most excellent OER catalytic activity (only 194 mV overpotential to obtain 10 mA cm^{-2} current density), which is much lower than the np-NiCoMnOOH (328 mV) and np-NiMnOOH (395 mV). Furthermore, it reaches the current density of 100 mA cm^{-2} at a meager overpotential of 292 mV. The performance of the np-NiMnOOH catalyst remains unimproved with the addition of Co, while the further addition of Fe markedly enhances the catalytic activity of np-NiCoMnOOH. Notably, the onset overpotential of np-NiFeCoMnOOH is considerably lower than that of RuO$_2$ (249 mV). Meanwhile, the LSV curves, without iR-corrected, also demonstrated the remarked OER activity of the electrocatalyst (Fig. S27).

Tafel slope is a crucial measure of electrochemical kinetics, as it reflect the speed at which a reaction occurs. As the Fig. 5b shows, np-NiFeCoMnOOH exhibits the lowest Tafel slope (67.96 mV dec^{-1}), which is much lower than that of np-NiMnOOH (186.91 mV dec^{-1}) and
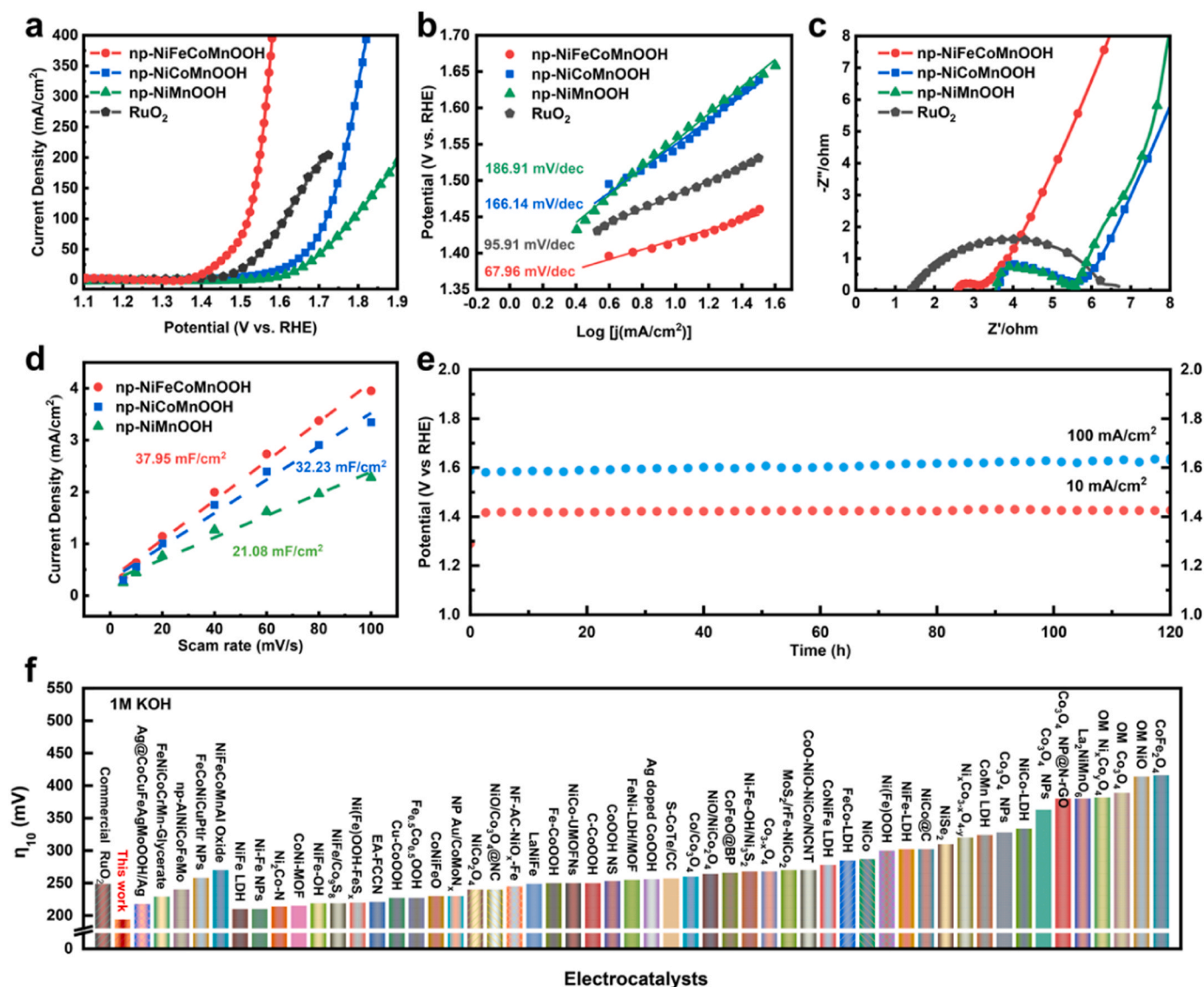

Fig. 5. Oxygen evolution reaction performance assessment. a OER linear sweep voltammetry (LSV), b Tafel plots curves and c EIS spectra of np-NiMnOOH, np-NiCoMnOOH and np-NiFeCoMnOOH electrocatalyst, as well as benchmark RuO$_2$ immobilized on glassy carbon electrode in 1 M KOH (electronic grade) with iR-corrected. Scan rate: 5 mV s^{-1}. d Double-layer capacitances (C$_{dl}$) of the np-NiMnOOH, np-NiCoMnOOH, np-NiFeCoMnOOH electrocatalyst. e Chronoamperometric (CP) test of the np-NiFeCoMnOOH electrocatalyst with 10 and 100 mA cm^{-2}. f Overpotentials at 10 mA cm^{-2} of np-NiFeCoMnOOH electrocatalyst, comparing with the other representative HE materials and Ni, Co and Fe-based materials.

np-NiCoMnOOH (166.14 mV dec^{-1}), and even surpasses the Tafel slope of RuO$_2$ (95.91 mV dec^{-1}). The diversity of Tafel slopes indicates that the addition of the element Fe in np-NiCoMnOOH effectively enhance the electrochemical reaction kinetics, suggesting the np-NiFeCoMnOOH catalysts may follow distinct OER reaction mechanisms and reaction pathways[46]. The charge transfer capacity between the electrocatalyst and the solution was assessed by the electrochemical impedance spectra (EIS) measure at the overpotential of 200 mV (Fig. 5c). The generally low charge transfer resistance (R$_{ct}$) comes mainly from the integral nature of the free-standing electrocatalyst and nanoporous structure of the electrocatalyst, which can effectively improve the efficiency of charge exchange during the electrochemical reaction [47,48]. Another critical parameter frequently used to evaluate the electrocatalytic activity is the electrochemically surface area (ECSA), which is calculated from the double-layer capacitance (C$_{dl}$). By performing the cyclic voltammetry (CV) measurements between 1.10 and 1.20 V vs. RHE at different scan rates (Fig. S28). As shown in the Fig. 5d, the np-NiFeCoMnOOH present the highest C$_{dl}$ of 37.95 mF cm^{-2}, but don't exhibit a significant advantage compared to np-NiCoMnOOH (32.23 mF cm^{-2}), This indicates that the excellent OER catalytic performance of np-NiFeCoMnOOH is due mainly to its intrinsic.

In practice, the stability is also an important aspect to evaluate the OER electrocatalysts, except of onset overpotential. As shown in the Fig. 5e, the result of chronopotentiometry (CP) tests indicate that np-NiFeCoMnOOH electrocatalysts have remarkable long-lasting stability because of the extremely small increase (5 mV) for overpotential in its current density at the 10 mA cm^{-2} after 120 h. Meanwhile, the performance of the catalyst also has a slight decay at high reaction rate (100 mA cm^{-2}) of stability test after the same time (Fig. S29). Notably, the catalysts remained in its original nanoporous structure and phase structure (Fig. S30), but with a slight growth of the NiFeCoMnOOH after the CP test (Fig. S31), indicating its excellent performance and structural stability. Meanwhile, the Ni, Fe, Co and Mn 2p peaks of the np-NiFeCoMnOOH electrode have not changed significantly during the surface reconstruction and the CP test, which means all of the metal components exhibit the beforehand oxidation during the dealloying process (Fig. S32). The presence of this pre-oxidation process facilitates the subsequent generation of (oxy)hydroxide during surface reconstruction [49]. Notably, the peaks of O 1 s occurs the obvious split during the in-situ activation. The deconvolution has three characteristic peaks at 529.6531.5 and 533.3 eV (labelled O-I, O-II and O-III) assigned to M-O, oxygen in M-OH, and H$_2$O, respectively. This apparent change is further evidence of the synthesis of HE (oxy)hydroxide during the surface reconstruction. Impressively, the oxygen evolution activity of np-NiFeCoMnOOH outperformed most HE OER electrocatalysts and other Ni, Co and Fe-based materials, as shown in the Fig. 5f.

4. Conclusion

Through theoretical calculations and experimental verification, we have successfully synthesized a high-entropy electrocatalyst with a nano-porous self-supporting structure. By employing targeted design of alloy composition, we have achieved directed modulation of the electrocatalytic reaction pathway. The DFT calculation results show that the addition of Fe element can effectively modulate the electronic distribution in high-entropy materials, thereby enhancing the covalent characteristics of M-O bonds, which should be responsible for the change in reaction pathways compared to other samples. Meanwhile, the np-NiFeCoMnOOH have a low overpotential of 194 mV at a density current of 10 mA cm^{-2} and remarkable long-term stability. Consistently, the in-depth study of the reaction mechanism is beneficial for improving the understanding of the source of catalytic activity of high entropy materials and, in turn, guiding the rational design and convenient synthesis of high entropy catalysts with high performance.

CRediT authorship contribution statement

Yimin Zhang: Conceptualization, Methodology, Writing – original draft. **Jianli Kang:** Conceptualization, Writing – review & editing, Supervision. **Haonan Xie:** Validation. **Hongxia Yin:** Validation. **Zhijia Zhang:** Validation, Funding acquisition. **Enzuo Liu:** Validation, Project administration. **Liyin Ma:** Investigation, Validation. **Biao Chen:** Investigation, Validation. **Junwei Sha:** Investigation, Validation. **Lihua Qian:** Validation, Project administration. **Wenbin Hu:** Validation, Project administration. **Chunnian He:** Validation, Project administration. **Naiqin Zhao:** Conceptualization, Writing – review & editing, Supervision.

Declaration of Competing Interest

The authors declare that they have no known competing financial interests or personal relationships that could have appeared to influence the work reported in this paper.

Data Availability

Data will be made available on request.

Acknowledgements

Appendix A. Supporting information

Supplementary data associated with this article can be found in the online version at doi:10.1016/j.apcatb.2023.123331.

References

[1] P. De Luna, C. Hahn, D. Higgins, S.A. Jaffer, T.F. Jaramillo, E.H. Sargent, What would it take for renewably powered electrosynthesis to displace petrochemical processes? Science 364 (2019).
[2] J. Kibsgaard, I. Chorkendorff, Considerations for the scaling-up of water splitting catalysts, Nat. Energy 4 (2019) 430–433.
[3] H. Xie, B. Chen, C. Liu, G. Wu, C. Sui, E. Liu, G. Zhou, C. He, W. Hu, N. Zhao, Engineering the interfacial doping of 2D heterostructures with good bidirectional reaction kinetics for durably reversible sodium-ion batteries, Energy Storage Mater. 60 (2023).
[4] B. Chen, X. Zhong, G. Zhou, N. Zhao, H.M. Cheng, Graphene-supported atomically dispersed metals as bifunctional catalysts for next-generation batteries based on conversion reactions, Adv. Mater. 34 (2022), e2105812.
[5] M. Yu, E. Budiyanto, H. Tuysuz, Principles of water electrolysis and recent progress in cobalt-, nickel-, and iron-based oxides for the oxygen evolution reaction, Angew. Chem. Int Ed. Engl. 61 (2022), e202103824.
[6] J. Yu, B.-Q. Li, C.-X. Zhao, Q. Zhang, Seawater electrolyte-based metal–air batteries: from strategies to applications, Energy Environ. Sci. 13 (2020) 3253–3268.
[7] Z. Yan, J.L. Hitt, J.A. Turner, T.E. Mallouk, Renewable electricity storage using electrolysis, Proc. Natl. Acad. Sci. USA 117 (2020) 12558–12563.
[8] H.N. Nong, L.J. Falling, A. Bergmann, M. Klingenhof, H.P. Tran, C. Spori, R. Mom, J. Timoshenko, G. Zichittella, A. Knop-Gericke, S. Piccinin, J. Perez-Ramirez, B. R. Cuenya, R. Schlogl, P. Strasser, D. Teschner, T.E. Jones, Key role of chemistry versus bias in electrocatalytic oxygen evolution, Nature 587 (2020) 408–413.
[9] Y. Zhu, Z. He, Y. Choi, H. Chen, X. Li, B. Zhao, Y. Yu, H. Zhang, K.A. Stoerzinger, Z. Feng, Y. Chen, M. Liu, Tuning proton-coupled electron transfer by crystal orientation for efficient water oxidization on double perovskite oxides, Nat. Commun. 11 (2020) 4299.
[10] F. Dionigi, J. Zhu, Z. Zeng, T. Merzdorf, H. Sarodnik, M. Gliech, L. Pan, W.X. Li, J. Greeley, P. Strasser, Intrinsic electrocatalytic activity for oxygen evolution of crystalline 3d-transition metal layered double hydroxides, Angew. Chem. Int Ed. Engl. 60 (2021) 14446–14457.
[11] A. Grimaud, O. Diaz-Morales, B. Han, W.T. Hong, Y.L. Lee, L. Giordano, K. A. Stoerzinger, M.T.M. Koper, Y. Shao-Horn, Activating lattice oxygen redox reactions in metal oxides to catalyse oxygen evolution, Nat. Chem. 9 (2017) 457–465.

[12] J.T. Mefford, X. Rong, A.M. Abakumov, W.G. Hardin, S. Dai, A.M. Kolpak, K.
P. Johnston, K.J. Stevenson, Water electrolysis on La(1-x)Sr(x)CoO(3-delta)
perovskite electrocatalysts, Nat. Commun. 7 (2016) 11053.

[13] Z.-F. Huang, J. Song, Y. Du, S. Xi, S. Dou, J.M.V. Nsanzimana, C. Wang, Z.J. Xu,
X. Wang, Chemical and structural origin of lattice oxygen oxidation in Co–Zn
oxyhydroxide oxygen evolution electrocatalysts, Nat. Energy 4 (2019) 329–338.

[14] N. Voronina, N. Yaqoob, H.J. Kim, K.S. Lee, H.D. Lim, H.G. Jung, O. Guillon,
P. Kaghazchi, S.T. Myung, A new approach to stable cationic and anionic redox
activity in O3–layered cathode for sodium-ion batteries, Adv. Energy Mater. 11
(2021).

[15] R.R. Rao, M.J. Kolb, L. Giordano, A.F. Pedersen, Y. Katayama, J. Hwang, A. Mehta,
H. You, J.R. Lunger, H. Zhou, N.B. Halck, T. Vegge, I. Chorkendorff, I.E.
L. Stephens, Y. Shao-Horn, Operando identification of site-dependent water
oxidation activity on ruthenium dioxide single-crystal surfaces, Nat. Catal. 3
(2020) 516–525.

[16] A. Grimaud, A. Demortière, M. Saubanère, W. Dachraoui, M. Duchamp, M.-
L. Doublet, J.-M. Tarascon, Activation of surface oxygen sites on an iridium-based
model catalyst for the oxygen evolution reaction, Nat. Energy 2 (2016).

[17] M.N. Grisolia, J. Varignon, G. Sanchez-Santolino, A. Arora, S. Valencia, M. Varela,
R. Abrudan, E. Weschke, E. Schierle, J.E. Rault, J.P. Rueff, A. Barthelemy,
J. Santamaria, M. Bibes, Hybridization-controlled charge transfer and induced
magnetism at correlated oxide interfaces, Nat. Phys. 12 (2016) 484–492.

[18] R.H. Potze, G.A. Sawatzky, M. Abbate, Possibility for an intermediate-spin ground
state in the charge-transfer material SrCoO₃, Phys. Rev. B Condens Matter 51
(1995) 11501–11506.

[19] Y.Y. Chin, Z. Hu, H.J. Lin, S. Agrestini, J. Weinen, C. Martin, S. Hébert, A. Maignan,
A. Tanaka, J.C. Cezar, N.B. Brookes, Y.F. Liao, K.D. Tsuei, C.T. Chen, D.I. Khomskii,
L.H. Tjeng, Spin-orbit coupling and crystal-field distortions for a low-spin 3d5 state
in BaCoO3, Phys. Rev. B (2019) 100.

[20] R.A. House, J.-J. Marie, M.A. Pérez-Osorio, G.J. Rees, E. Boivin, P.G. Bruce, The
role of O2 in O-redox cathodes for Li-ion batteries, Nat. Energy 6 (2021) 781–789.

[21] D. Eum, B. Kim, J.H. Song, H. Park, H.Y. Jang, S.J. Kim, S.P. Cho, M.H. Lee, J.
H. Heo, J. Park, Y. Ko, S.K. Park, J. Kim, K. Oh, D.H. Kim, S.J. Kang, K. Kang,
Coupling structural evolution and oxygen-redox electrochemistry in layered
transition metal oxides, Nat. Mater. 21 (2022) 664–672.

[22] N. Zhang, Y. Chai, Lattice oxygen redox chemistry in solid-state electrocatalysts for
water oxidation, Energy Environ. Sci. 14 (2021) 4647–4671.

[23] Z. He, J. Zhang, Z. Gong, H. Lei, D. Zhou, N. Zhang, W. Mai, S. Zhao, Y. Chen,
Activating lattice oxygen in NiFe-based (oxy)hydroxide for water electrolysis, Nat.
Commun. 13 (2022) 2191.

[24] L. Tang, Y. Yang, H. Guo, Y. Wang, M. Wang, Z. Liu, G. Yang, X. Fu, Y. Luo,
C. Jiang, Y. Zhao, Z. Shao, Y. Sun, High configuration entropy activated lattice
oxygen for o2 formation on perovskite electrocatalyst, Adv. Funct. Mater. (2022).

[25] Y. Wu, Y. Zhao, P. Zhai, C. Wang, J. Gao, L. Sun, J. Hou, Triggering the lattice
oxygen activation of single-atomic Mo sites anchored Ni-Fe oxyhydroxides
nanoarrays for electrochemical water oxidation, Adv. Mater. (2022), e2202523.

[26] X. Chen, Q. Wang, Y. Cheng, H. Xing, J. Li, X. Zhu, L. Ma, Y. Li, D. Liu, S-doping
triggers redox reactivities of both iron and lattice oxygen in FeOOH for low-cost
and high-performance water oxidation, Adv. Funct. Mater. (2022).

[27] Z.F. Huang, S. Xi, J. Song, S. Dou, X. Li, Y. Du, C. Diao, Z.J. Xu, X. Wang, Tuning of
lattice oxygen reactivity and scaling relation to construct better oxygen evolution
electrocatalyst, Nat. Commun. 12 (2021) 3992.

[28] Y.-J. Ko, M.H. Han, C. Lim, S.-H. Yu, C.H. Choi, B.K. Min, J.-Y. Choi, W.H. Lee, H.-
S. Oh, Unveiling the role of Ni in Ru-Ni oxide for oxygen evolution: lattice oxygen
participation enhanced by structural distortion, J. Energy Chem. (2022).

[29] T. Zhang, H. Huang, J. Han, F. Yan, C. Sun, Manganese-doped hollow layered
double (Ni, Co) hydroxide microcuboids as an efficient electrocatalyst for the
oxygen evolution reaction, ChemElectroChem 7 (2020) 3852–3858.

[30] R. Zhang, L. Huang, Z. Yu, R. Jiang, Y. Hou, L. Sun, B. Zhang, Y. Huang, B. Ye,
Y. Zhang, Spherical cactus-like composite based on transition metals Ni, Co and Mn
with 1D / 2D bonding heterostructure for electrocatalytic overall water splitting,
Electrochim. Acta 323 (2019).

[31] L. Tao, M. Sun, Y. Zhou, M. Luo, F. Lv, M. Li, Q. Zhang, L. Gu, B. Huang, S. Guo,
A general synthetic method for high-entropy alloy subnanometer ribbons, J. Am.
Chem. Soc. (2022).

[32] Z. Jia, T. Yang, L. Sun, Y. Zhao, W. Li, J. Luan, F. Lyu, L.C. Zhang, J.J. Kruzic, J.
J. Kai, J.C. Huang, J. Lu, C.T. Liu, A novel multinary intermetallic as an active
electrocatalyst for hydrogen evolution, Adv. Mater. 32 (2020), e2000385.

[33] M. Cui, C. Yang, B. Li, Q. Dong, M. Wu, S. Hwang, H. Xie, X. Wang, G. Wang, L. Hu,
High-entropy metal sulfide nanoparticles promise high-performance oxygen
evolution reaction, Adv. Energy Mater. (2020).

[34] A. Grimaud, W.T. Hong, Y. Shao-Horn, J.M. Tarascon, Anionic redox processes for
electrochemical devices, Nat. Mater. 15 (2016) 121–126.

[35] S. Tian, Q. Zeng, G. Liu, J. Huang, X. Sun, D. Wang, H. Yang, Z. Liu, X. Mo,
Z. Wang, K. Tao, S. Peng, Multi-dimensional composite frame as bifunctional
catalytic medium for ultra-fast charging lithium-sulfur battery, Nanomicro Lett. 14
(2022) 196.

[36] I. Abate, S.Y. Kim, C.D. Pemmaraju, M.F. Toney, W. Yang, T.P. Devereaux, W.
C. Chueh, L.F. Nazar, The role of metal substitution in tuning anion redox in
sodium metal layered oxides revealed by x-ray spectroscopy and theory, Angew.
Chem. Int. Ed. Engl. 60 (2021) 10880–10887.

[37] J. Hu, A. Al-Salihy, J. Wang, X. Li, Y. Fu, Z. Li, X. Han, B. Song, P. Xu, Improved
interface charge transfer and redistribution in CuO-CoOOH p-n heterojunction
nanoarray electrocatalyst for enhanced oxygen evolution reaction, Adv. Sci. 8
(2021), e2103314.

[38] P. Guo, S. Cao, Y. Wang, X. Lu, Y. Zhang, X. Xin, X. Chi, X. Yu, I. Tojiboyev,
H. Salari, A.J. Sobrido, M. Titirici, X. Li, Surface self-reconstruction of telluride
induced by in-situ cathodic electrochemical activation for enhanced water
oxidation performance, Appl. Catal. B: Environ. 310 (2022).

[39] M.W. Louie, A.T. Bell, An investigation of thin-film Ni-Fe oxide catalysts for the
electrochemical evolution of oxygen, J. Am. Chem. Soc. 135 (2013) 12329–12337.

[40] X. Wang, S. Xi, P. Huang, Y. Du, H. Zhong, Q. Wang, A. Borgna, Y.W. Zhang,
Z. Wang, H. Wang, Z.G. Yu, W.S.V. Lee, J. Xue, Pivotal role of reversible NiO₆
geometric conversion in oxygen evolution, Nature (2022).

[41] R. Li, X.J. Liu, H. Wang, D.Q. Zhou, Y. Wu, Z.P. Lu, Formation mechanism and
characterization of nanoporous silver with tunable porosity and promising
capacitive performance by chemical dealloying of glassy precursor, Acta Mater.
105 (2016) 367–377.

[42] H.J. Qiu, J.L. Kang, P. Liu, A. Hirata, T. Fujita, M.W. Chen, Fabrication of large-
scale nanoporous nickel with a tunable pore size for energy storage, J. Power
Sources 247 (2014) 896–905.

[43] K.Y. Li, D.F. Xue, Estimation of electronegativity values of elements in different
valence states, J. Phys. Chem. A 110 (2006) 11332–11337.

[44] C. Cheng, C. Chen, S. Chu, H. Hu, T. Yan, X. Xia, X. Feng, J. Guo, D. Sun, J. Wu,
S. Guo, L. Zhang, Enhancing the reversibility of lattice oxygen redox through
modulated transition metal-oxygen covalency for layered battery electrodes, Adv.
Mater. 34 (2022), e2201152.

[45] C. Wei, Z.J. Xu, The comprehensive understanding of 10 mA cm$_{geo}^{-2}$ as an evaluation
parameter for electrochemical water splitting, Small Methods 2 (2018).

[46] A. Moysiadou, S. Lee, C.S. Hsu, H.M. Chen, X. Hu, Mechanism of oxygen evolution
catalyzed by cobalt oxyhydroxide: cobalt superoxide species as a key intermediate
and dioxygen release as a rate-determining step, J. Am. Chem. Soc. 142 (2020)
11901–11914.

[47] H. Liu, C. Xi, J. Xin, G. Zhang, S. Zhang, Z. Zhang, Q. Huang, J. Li, H. Liu, J. Kang,
Free-standing nanoporous NiMnFeMo alloy: an efficient non-precious metal
electrocatalyst for water splitting, Chem. Eng. J. 404 (2021).

[48] H. Shi, Y.T. Zhou, R.Q. Yao, W.B. Wan, X. Ge, W. Zhang, Z. Wen, X.Y. Lang, W.
T. Zheng, Q. Jiang, Spontaneously separated intermetallic Co₃Mo from nanoporous
copper as versatile electrocatalysts for highly efficient water splitting, Nat.
Commun. 11 (2020) 2940.

[49] D. Zhao, M. Dai, Y. Zhao, H. Liu, Y. Liu, X. Wu, Improving electrocatalytic activities
of FeCo₂O₄@FeCo₂S₄@PPy electrodes by surface/interface regulation, Nano
Energy 72 (2020).